vortex. Its circulation is on the order of one-fifth of the circulation of the primary (incident) vortex.

Near the leading region of the tail, the primary–secondary (counter) vortex system is highly coherent. The instantaneous vortex patterns deviate only slightly from the time-averaged representations. Furthermore, locations of peak values of velocity fluctuation and Reynolds stress occur at the interface between the primary and secondary vortices on the outboard side of the tail.

Evolution of this vortex pattern along the tail is associated with a degeneration of coherence of the primary–secondary vortex system. That is, the instantaneous states deviate significantly from the time-averaged pattern of the primary–secondary vortex system.

In the trailing region of the tail, peak values of velocity fluctuation and Reynolds stress are still detectable at the interface between the primary and secondary vortex on the outboard side of the tail. However, in addition, severe distortion of the primary vortex about the tail results in additional peaks of velocity fluctuation and Reynolds stress on the inboard side.

Acknowledgments

The authors gratefully acknowledge support of this research under U.S. Air Force Office of Scientific Research Grants F49620-00-1-0009 and F49620-02-1-0061, monitored by Steven Walker and John Schmisseur. In addition, supplemental funding for instrumentation was provided by U.S. Office of Naval Research Grants N00014-99-1-0581 and N0014-01-1-0606.

References

[1]Rockwell, D., "Vortex Body Interactions," *Annual Review of Fluid Mechanics*, Vol. 30, 1998, pp. 199–229.

[2]Menke, M., and Gursul, I., "Unsteady Nature of Leading Edge Vortices," *Physics of Fluids*, Vol. 9, No. 10, 1997, pp. 2610–2616.

[3]Garg, A. K., and Leibovich, S., "Spectral Characteristics of Vortex Breakdown Flowfields," *Physics of Fluids*, Vol. 22, No. 11, 1979, pp. 2053–2064.

[4]Gursul, I., "Unsteady Flow Phenomena over Delta Wings at High Angle of Attack," *AIAA Journal*, Vol. 32, No. 2, 1994, pp. 225–231.

[5]Gursul, I., and Yang, H., "On Fluctuations of Vortex Breakdown Location," *Physics of Fluids*, Vol. 7, No. 1, 1995, pp. 229–231.

[6]Beutner, T. J., Baust, H. N., and Meyers, J. F., "Doppler Global Velocimetry Measurements of a Vortex–Tail Interaction," *Proceedings of the 7th International Symposium on Flow Visualization*, edited by J. P. Crowder, Begell House, New York, 1995, pp. 418–423.

[7]Canbazoglu, S., Lin, J.-C., Wolfe, S., and Rockwell, D., "Buffeting of Fin: Distortion of Incident Vortex," *AIAA Journal*, Vol. 33, No. 11, 1995, pp. 2144–2150.

[8]Canbazoglu, S., Lin, J.-C., Wolfe, S., and Rockwell, D., "Buffeting of Fin: Streamwise Evolution of Flow Structure," *Journal of Aircraft*, Vol. 33, No. 1, 1995, pp. 185–190.

[9]Rizk, Y. M., and Gee, K., "Unsteady Simulation of Viscous Flowfield Around F-18 Aircraft at Large Incidence," *Journal of Aircraft*, Vol. 29, No. 6, 1992, pp. 986–992.

[10]Gee, K., Murman, S. M., and Schiff, L. B., "Computational Analysis of F/A-18 Tail Buffet," AIAA Paper 95-3440, Aug. 1995.

[11]Kandil, O. A., Sheta, E. F., and Massey, S. J., "Buffet Responses of a Vertical Tail in Vortex Breakdown Flows," AIAA Paper 95-3464, Aug. 1995.

[12]Rizzetta, D. P., "Numerical Simulation of the Interaction Between a Leading-Edge Vortex in a Vertical Tail," AIAA Paper 96-2012, June 1996.

[13]Wolfe, S., Canbazoglu, S., Lin, J.-C., and Rockwell, D., "Buffeting of Fins: Assessment of Surface Pressure Loading," *AIAA Journal*, Vol. 33, No. 11, 1995, pp. 2232–2235.

[14]Mayori, A., and Rockwell, D., "Interaction of a Streamwise Vortex with a Thin Plate: A Source of Turbulent Buffeting," *AIAA Journal*, Vol. 32, No. 10, 1994, pp. 2022–2029.

[15]Gordnier, R. E., and Visbal, M. R., "Numerical Simulation of the Impingement of a Streamwise Vortex on a Plate," AIAA Paper 97-1781, June–July 1997.

[16]Washburn, A. E., Jenkins, L. M., and Ferman, M. A., "Experimental Investigation of Vortex–Fin Interaction," AIAA Paper 93-0050, Jan. 1993.

A. Plotkin
Associate Editor

Autonomous Gain-Phase Tailoring of Rotational Acceleration Rate Sensors

Yu-Hsiang Hsu* and Chih-Kung Lee†
National Taiwan University,
Taipei 106, Taiwan, Republic of China

Nomenclature

c = elastic stiffness constants
D = electric displacement
d = piezoelectric strain/charge constant
E = electrical field
e = piezoelectric stress/charge constant
G = shear modulus
k = wave number
q = surface charge
r = radius of the shaft
S = strain
T = stress
u = displacement along x direction
v = displacement along y direction
ε = permittivity
θ = twisting angle
ρ = density
ω = frequency

Introduction

THE original concept of spatial filter, first reported in 1990,[1] was based on a distributed piezoelectric sensor that introduced a no-phase delay low-pass filter to the sensor transfer function. This spatial filter could only be placed far from the boundaries of a free-free plate and was required to be smaller in size when compared with the attached structure. The underlying reason for the spatial filter to be placed at locations far from the boundaries was to avoid the effect of evanescent waves and the effect of the boundaries, that is, only propagating waves were to be considered. Even with those restrictions, these earlier spatial filters did successfully introduce a no-phase delay low-pass filter to the sensor transfer that at first glance seems to conflict with the Bode gain-phase theorem. More specifically, spatial filters appear to offer a valid approach to introducing autonomous behavior into sensor transfer functions. As a rod can be modeled by using a second-order partial differential equation, only two propagating waves are needed to examine their dynamic behaviors.[2] A newly developed methodology that extends the earlier spatial wave concept to include finite structures or structures with sizes comparable to that of the sensor size will be introduced. With the capability to handle boundary effects and then utilizing the fact that only propagating wave modes are present within a rod, a rotational acceleration rate sensor that uses a rod as its base structure was developed to demonstrate bandwidth expansion capabilities when a distributed sensor design is integrated with a traditional point sensor. The theory, experimental results, related design, and performance implications on this newly invented rotational acceleration rate sensor will be detailed in this Note.

Theory of Piezoelectric Laminates

The constitutive equations of piezoelectric materials are[3]

$$S_p = s^E_{pq} T_q - d_{ip} E_i, \qquad D_i = d_{ip} T_q + \varepsilon^T_{ij} E_k \tag{1}$$

Received 24 August 2001; revision received 10 April 2002; accepted for publication 17 April 2002. Copyright © 2002 by the American Institute of Aeronautics and Astronautics, Inc. All rights reserved. Copies of this paper may be made for personal or internal use, on condition that the copier pay the $10.00 per-copy fee to the Copyright Clearance Center, Inc., 222 Rosewood Drive, Danvers, MA 01923; include the code 0001-1452/03 $10.00 in correspondence with the CCC.

*Graduate Research Assistant, Institute of Applied Mechanics.
†Professor, Institute of Applied Mechanics. Senior Member AIAA.

where $i, k = 1 \sim 3$ and $p, q = 1 \sim 6$. Equation (1) clearly shows that piezoelectric material is an electrical and mechanical fully coupled media. Because a 52-μm-thick PVF_2 thin film was used as the piezoelectric sensor material to verify this new concept, a plane stress approximation was adopted to simplify the constitutive equations of this class 6-mm piezoelectric material to become[4]

$$D_{3'} = \varepsilon_{3'3'} E_{3'} + d_{3'1'} T_{1'} + d_{3'2'} T_{2'} + d_{3'6'} T_{6'} \tag{2}$$

where the notation "$'$" represents the constants as referred to by the material coordinate axes and d_{36} represents the induced electrical displacement when a unit shear stress $T_{6'}$, that is, σ_{xy} in normal elasticity representations, was applied to the piezoelectric material. Using Gauss's law to find the signals detectable by the surface electrode $S^{(12)}$, we can determine the charge signals generated by the kth lamina[4]:

$$q(t) = \iint_{S^{(12)}} R(x, y) \left[e_{31} \frac{\partial u}{\partial x} + e_{32} \frac{\partial v}{\partial y} + e_{36} \left(\frac{\partial u}{\partial y} + \frac{\partial v}{\partial x} \right) \right] \mathrm{d}x\, \mathrm{d}y \tag{3}$$

where $R(x, y)$ is the effective surface electrode. We know that the governing equation of a one-dimensional circular rod in torsional motion is[2]

$$G \frac{\partial^2 \theta(x,t)}{\partial x^2} - \rho \frac{\partial^2 \theta(x,t)}{\partial t^2} = 0 \tag{4}$$

Considering only a time harmonic motion, that is, $\theta(x, t) = \theta(x) e^{i\omega t}$ and $j = (-1)^{(1/2)}$, Eq. (4) then becomes

$$\frac{\partial^2 \theta(x)}{\partial x^2} + k^2 \theta(x) = 0 \tag{5}$$

where

$$k^2 = -(\rho/G)\omega^2 \tag{6}$$

is the dispersion relationship between frequency ω and wave number k. The general solution of an one-dimensional rod thus becomes

$$\theta(x, t) = \left[w_{\mathrm{lp}} e^{jkx} + w_{\mathrm{rp}} e^{-jkx} \right] e^{jwt} \tag{7}$$

where w_{lp} and w_{rp} are the wave mode amplitudes of the left and the right propagating waves. These wave mode amplitudes are determined by the boundary conditions of the rod and the origin of the coordinate axis chosen, that is, the characteristics of the structure and the local information of the origin are embedded in these wave mode amplitudes. The chosen origin is named as the targeted origin to signify its influence to the spatial filter performance herein. As the piezoelectric thin film was attached to the surface of this one-dimensional rod, it experienced pure shear strain $\varepsilon_{\theta z} = r\, \mathrm{d}\theta/\mathrm{d}x$ only. Substituting Eq. (7) into Eq. (3) leads to the sensor equation where

$$q_s(k) = jke_{36} r^2 \int_0^a R(x) \left[w_{\mathrm{lp}} e^{jkx} - w_{\mathrm{rp}} e^{-jkx} \right] \mathrm{d}x \tag{8}$$

The sensor transfer function can be tailored by choosing a proper effective surface electrode $R(x)$. More specifically, $R(x)$ serves as a weighting function applied to the measured strain distribution. It can be shown that propagating wave modes within an one-dimensional shaft can be expanded into infinite domain by introducing the concept of the method of imaging.[5] With the introduction of the method of imaging, spatial filters represented by Eq. (8) can be evaluated by using a two-sided Laplace transform[6] as was done previously.[1]

Implementing a Rotational Acceleration Rate Sensor

Figure 1 shows the schematic adopted to expand a wave mode of an one-dimensional clamp-free rod to the infinite domain by the method of imaging.[7] Note that wave modes are odd and even functions with respect to the fixed and the free ends, respectively. For the spatial filter shown in Fig. 1 with a targeted origin placed at the fixed end, it has an odd function with respect to the origin when examined from the infinite domain. Because the spatial filter is antisymmetric with respect to the origin in the infinite domain, the sensor equation can be further reduced to

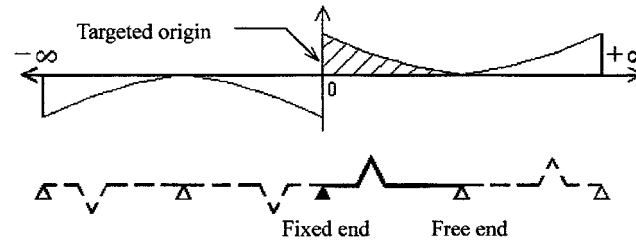

Fig. 1 Schematic of extending a propagating wave into infinite domain with a spatial filter by using the method of imaging.

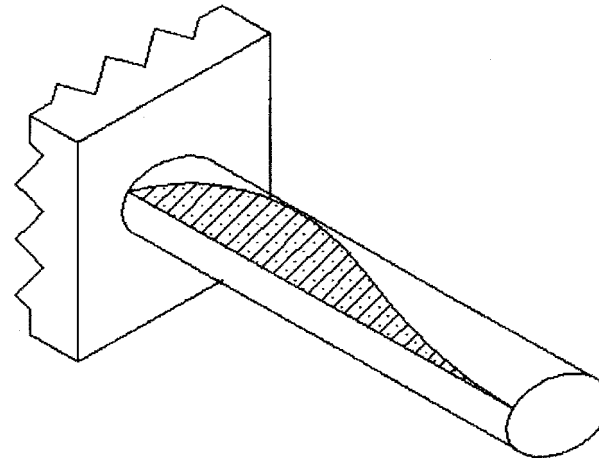

Fig. 2 Schematic of a spatial filter on an one-dimensional rod.

$$q_s(k) = jke_{36} r^2 (w_{\mathrm{lp}} - w_{\mathrm{rp}}) \int_{-\infty}^{\infty} R_o(x) e^{-jkx}\, \mathrm{d}x \tag{9}$$

where subscript o represents the spatial filter as an odd function in the infinite domain. Choosing an effective surface electrode $R_o(x)$ as $e^{-\alpha x} - e^{-\beta x} - C \sin(\gamma x)$ from 0 to a like the one shown in Fig. 2 and then substituting the dispersion relationship Eq. (6) into Eq. (9) leads to

$$q(k) = jke_{36} r^2 (w_{\mathrm{lp}} - w_{\mathrm{rp}}) \left(\frac{G}{\rho} \right)^{\frac{1}{2}} \left[\frac{(\bar{\beta}^2 - \bar{\alpha}^2) j\omega}{(\bar{\alpha}^2 + \omega^2)(\bar{\beta}^2 + \omega^2)} \right] \tag{10}$$

which is that of an −60-dB/decade low-pass filter in the frequency domain. The two second-order poles in the denominator do not introduce any phase lag into the sensor transfer function, and a 90-deg phase lead was introduced by the first-order zero from the numerator. The odd function spatial filter in infinite domain induced this first-order zero, which equals a differentiation in frequency domain mathematically.[5] Physically, measuring the charge output of a spatial filter with the targeted origin placed at a fixed end established a rotational acceleration rate sensor.

Experimental Results

To verify the effect of the newly developed spatial filter that can be placed on a finite structure, a 50-mm-long silica gel one-dimensional rod with a 10-mm diameter was chosen as the sensor structure. The corner frequency γ of the sine function of the effective surface electrode $R_o(x)$ was chosen to be 95 Hz, and the corner frequency α and β were chosen to be 200 and 250 Hz, respectively. Figure 3 compares the rotational accelerometer transfer function for the designed spatial filter to that of an uniform sensor. It is clear from Fig. 3 that introducing a −60-dB/decade low-pass filter by using the newly developed spatial filter flattens the bandwidth of the rotational sensor, and a 90-deg phase lead was also introduced by the induced zero.

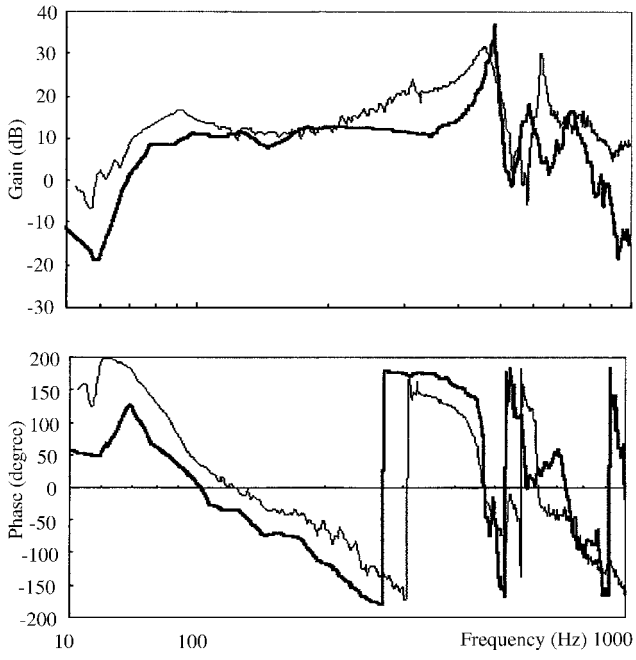

Fig. 3 Transfer function of a rotational accelerometer based on a spatial filter (——) and uniform sensor (——) design.

This experimental result clearly verifies the possibility of enhancing the bandwidth of a rotational acceleration rate sensor by adopting a concept of spatial filters.

Conclusions

The concept and design freedom introduced by adopting spatial filters to second-order partial differential equation systems have been successfully verified by an one-dimensional clamped-free shaft-based rotational acceleration rate sensor. It was shown that spatial filters can introduce a no-phase delay low-pass filter by offering a weighting function with the prechosen surface electrode, and the introduction of this odd function brings a differentiation to the transfer function. The method of imaging was introduced to extend the spatial filter application area from a finite structure to an infinite domain, that is, spatial filters can now be placed near or even at the boundaries. Benefits associated with adopting spatial filters to point sensors successfully demonstrate theoretically as well as experimentally the advantages of the newly developed rotational acceleration rate sensor. In summary, expanding the bandwidth of rotational acceleration rate sensors by using newly developed finite domain spatial filters has been successfully verified both theoretically and experimentally.

References

[1]Miller, D. W., Collins, S. A., and Peltzman, S. P., "Development of Spatially Convolving Sensors for Structural Control Applications," *Proceedings of the AIAA/ASME/ASCE/AHS Structures, Structural Dynamics, and Materials Conference*, edited by B. Prasad, Pt. 4, AIAA, Washington, DC, 1990, pp. 2283–2297.

[2]Meirovitch, L., *Element of Vibration*, McGraw–Hill, New York, 1986, pp. 269, 270, 290–296.

[3]Cady, W. G., *Piezoelectricity*, Vol. 1, McGraw–Hill, New York, 1946, pp. 1–8.

[4]Lee, C. K., "Theory of Laminated Piezoelectric Plates for the Design of Distributed Sensors/Actuators: Part I. Governing Equations and Reciprocal Relationships," *Journal of the Acoustical Society of America*, Vol. 87, No. 3, 1990, pp. 1144–1158.

[5]Hsu, Y. H., and Lee, C. K., "Targeted Origin Placement for the Autonomous Gain-Phase Tailoring of Piezoelectric Sensors," *Smart Materials and Structures*, Vol. 11, No. 3, 2002, pp. 444–458.

[6]Oppenheim, A. V., and Schafer, R. W., *Signal and System*, Prentice–Hall, Upper Saddle River, NJ, 1999, pp. 655–692.

[7]Graff, K. F., *Wave Motion in Elastic Solids*, Dover, New York, 1975, pp. 80–82.

A. Berman
Associate Editor

Assessment of Delamination Fracture Load of Stringer Stiffened Composite Panel

R. Ramesh Kumar,* K. S. Praveen,†
and G. Venkateswara Rao‡
Vikram Sarabhai Space Center,
Thiruvananthapuram 695 022, India

Introduction

STRUCTURAL efficiency is an important aspect in the design of weight-conscious and cost-effective aerospace structures. This can be accomplished in many instances as in the case of stiffness-based design by increasing the stiffness through the use of stringers in the form of hat stiffeners. Efficient use of such composite panels requires that the panels be designed to operate at loads several times their initial buckling load. The composite stiffened panels are normally fabricated by cocuring the skin and stiffener or by bonding the precured stiffener to the skin. Under compressive loading it might fail either by delamination of stringer from the base panel, buckling, or delamination followed by buckling once its compression strength is higher than critical buckling load. The most common failure mode reported in the literature is separation of the stiffener from base panel as a delamination mode of failure.[1–6] However, the effect of this delamination on the failure load of the structure requires major research, and few reports are available in the literature.

In the present work failure is defined as an onset of delamination fracture resulting in separation of the stringer from the panel. One can conclude that for a stringer stiffened panel the most commonly observed failure mode under compressive loading is the delamination fracture. Once a delamination is present, the state of the art is to assess strain energy release rate G and compare it with its critical value Gc to evaluate the margin of safety. So it is essential to assess first the critical buckling load and then the possible damage caused by delamination, and only then can one estimate the margin of safety of the structure accurately. But as of today the aspect of "when a delamination analysis is to be considered" is not fully established in the literature.

The aim of the present study is first to predict the delamination fracture load of a compressively loaded stringer stiffened composite panel based on the strain energy release rate approach and then compare the fracture load thus obtained with both the test data for the failure load and the critical buckling load to assess the integrity of the structure. Finite element analyses are carried out to compare the strains determined from the geometric nonlinear analysis with test data to determine the critical buckling load and the delamination fracture load.

Description of the Test Panel

A composite panel of size 400×750 mm with four hat-type stringer stiffeners cocured with the skin (panel) on one side of the panel is shown in Fig. 1. The top and bottom part of the panel are locally reinforced over length of 50 mm and bolted to an aluminum T-channel section as shown in Fig. 1, which can go through the slit provided in the test setup. The top of the panel is immovable with the test fixture, whereas the bottom is movable in the vertical direction. The structure is made up of M55J/M18 carbon-epoxy prepreg.

Received 21 June 2001; revision received 3 September 2002; accepted for publication 3 September 2002. Copyright © 2002 by the American Institute of Aeronautics and Astronautics, Inc. All rights reserved. Copies of this paper may be made for personal or internal use, on condition that the copier pay the $10.00 per-copy fee to the Copyright Clearance Center, Inc., 222 Rosewood Drive, Danvers, MA 01923; include the code 0001-1452/03 $10.00 in correspondence with the CCC.

*Engineer, Structural Engineering Group.
†Graduate Student; currently Senior Development Engineer, Ashok Leyland, Technical Centre, Chennai 600 101, India.
‡Group Director, Structural Engineering Group.